Supporting Information

Nitrate Reduction to Ammonium: From CuO Defect Engineering to Waste NO_x-to-NH_3 Economic Feasibility

Rahman Daiyan*,[1] Thanh Tran-Phu,[2] Priyank Kumar,[1] Kevin Iputera,[3] Zizheng Tong,[3] Joshua Leverett,[1] Muhammad Haider Ali Khan,[1] Ali Asghar Esmailpour,[1] Ali Jalili,[1] Maggie Lim,[1] Antonio Tricoli,[2] Ru-Shi Liu*,[3] Xunyu Lu,[1] Emma Lovell*,[1] Rose Amal*[1]

[1]Particles and Catalysis Research Laboratories and School of Chemical Engineering, UNSW Sydney, Sydney, NSW 2052, Australia

[2] Nanotechnology Research Laboratory, Faculty of Engineering University of Sydney, NSW 2006 and Nanotechnology Research Laboratory, Research School of Chemistry, College of Science, The Australian National University, Canberra, ACT 2601, Australia

[3] Department of Chemistry, National Taiwan University, Taipei 106, Taiwan

* Corresponding authors
r.amal@unsw.edu.au
e.lovell@unsw.edu.au
rsliu@ntu.edu.tw

1. DFT Methods

We used the plane-wave VASP code for all our DFT calculations.[1–3] The core electrons in our calculations were treated using the projector augmented wave method (PAW) method,[1] and the Perdew-Burke-Ernzerhof (PBE) exchange-correlation functional[4] was employed. The cut-off value for the wavefunctions was set to 500 eV and a gamma-point k-grid was used. Relaxation calculations ended when the residual forces on atoms were less than 0.03 eV/Å. A vacuum region greater than 10 Å in the direction normal to the sheets was used to avoid interactions between periodic images.

We employed a CuO (111) surface slab containing 64 Cu and 64 O atoms (a=12.70 Å, b=11.87 Å, c=23.3 Å, α=73.7°, β=122.6°, γ=78.6°, where c is the surface normal direction) to simulate NO_xRR and HER active sites. One, two and three OVs were created to study the effect of defects on the catalytic processes (**see Figure 1c**). The free energy changes were computed using the computational hydrogen electrode (CHE) approach,[5] where the free energy of $(H^+ + e^-)$ equals $\frac{1}{2}H_2(g)$ for a standard hydrogen electrode (SHE). The free energy of various intermediates is calculated as:

$$G = E_{elec} + E_{ZPE} - TS$$

where, E_{elec} is the total electronic energy computed by DFT; E_{ZPE} is the zero-point energy (ZPE), T is temperature and S is entropy. For H adsorption, the change in free energy is computed as $\Delta G = \Delta E_{elec} + 0.24$ eV, where the value 0.24 eV, taken from ref.,[6] includes the corrections to the ZPE and the entropy terms. For the NORR intermediates, the correction terms were neglected – this, however, does not affect the key conclusions drawn from our DFT calculations.

We avoided using the charged NO_3^- species as a reference in our DFT calculations, while instead employing neutral HNO_3 as the gas-phase reference. The energy of NO_3^- ion was obtained using the reference values for the ionization energy of H and the heat of reaction for HNO_3 (gas) deprotonation, as detailed in ref.[7]

2. Technoeconomic Modelling Methods

A. Electrolyser Model

To model the 10 MW electrolyser system, we calculated the electrolyser area that would be required based on the performance data of pCuO-5 (**Figure 2**). This performance data is also used to calculate the overall energy and mass balance of the system. These collective data are used to establish the system capital (dependent on stack area) and operating costs (dependent on feedstock and electricity consumption). The mathematical model is represented below and is based on the framework developed by Jouny *et al*[8] and Jonggeol Na *et al*[9]. Note that we do not consider product separation, which is beyond the scope of our work.

Electrode Area

Based on the cell voltage (ΔV), we can determine the amount of current that will be passing through the electrolyser stack at the applied power of 10 MW (P). This current can then be correlated with the current density (*j*) of the system to determine the required electrolyser stack area as shown below:

$$P = \Delta V \times I_o \quad (1)$$

$$I_o = \frac{P}{\Delta V} \quad (2)$$

$$A_{Stack} = \frac{I_o}{j} \quad (3)$$

Here P is the installed power rating in Watts (W), ΔV is the cell potential in Volts (V), I_o is the current passing through the electrode in Amperes (A) and *j* is the current density in A m^{-2}.

Mass – Energy Balance

To carry out a mass and energy balance, we calculate the partial current for NO_xRR and utilize this to calculate the mass flowrate of the product as follows:

$$I_p = I_o \times FE_{NH4+} \quad (4)$$

$$F_{NH4+} = \frac{I_p}{e \times F_c} \times MW_x \quad (5)$$

Where, I_p is the partial current for NH_4^+, FE_{NH4^+} is the Faradaic efficiency, e is the number of electrons transferred to generate 1 mole of NH_4^+, MW_x is the molecular weight, F_c represents the Faraday's Constant (96,485 C mol^{-1}) and F_{NH4^+} represents the mass flowrate of NH_4^+ in g s^{-1}.

The NH_4^+ yield is calculated as follows:

$$Y_{NH4+} = \frac{F_X}{A_{Stack}} \quad (6)$$

Where, F_x is the flowrate of NH_4^+ in g h^{-1}, A_{stack} represents the electrolyser stack area in m^2 and the yield of NH_4^+ is represented by Y_{NH4^+} as g m^{-2} h^{-1}.

B. Electrolyser System Cost

Electrolyser System Capital Cost (CAPEX)

To determine the electrolyser capital cost, we correlate a reference area-based unit cost ($ m^{-2}) with the electrolyser stack area. These reference area-based costs are adopted from the US DOE H2A analysis for current distributed PEM electrolyser system[10]. A cost of \$342 kW^{-1} is used for an electrolyser stack that operates at a current density of 2 A cm^{-2} and cell voltage of 1.9 V. This reference cost for the PEM electrolyser is determined as:

$$Ref_{Cost} = \frac{\$342}{kW} \times \frac{2\ A}{cm^2} \times 1.9\ V \times \frac{10^4\ cm^2}{m^2} \times \frac{kW}{1000\ W} = 12{,}996\ \frac{\$}{m^2} \quad (7)$$

This reference cost is then used to estimate the cost of NO_xRR electrolyser stack cost. For our calculations, we assume that a commercial PEM electrolyser can be easily retrofitted to operate for NO_xRR. In addition, on the basis of DOE estimate, we assume that the BoP of NO_xRR electrolyser will be 43% of total system cost with 57% due to stack cost.[10]

Electrolyser System Operating Cost (OPEX)

Electricity Price

For our analysis, we use electricity prices from the International Renewable Energy Agency (IRENA) and International Energy Agency (IEA) to include global weighted average electricity prices for grid supplied electricity for both fossil-based as well as for renewable power purchase agreements (PPA).[11,12] The grid electricity, solar PPA and wind PPA considered herein are \$97 MWh^{-1} (97% capacity factor), \$68 MWh^{-1} (18% capacity factor) and \$53 MWh^{-1} (51%), respectively. For the solar and wind PPAs, the intermittency of the solar and wind generation will limit the operational capacity of the electrolyser. The capacity factor (c_f) represents the ratio of the actual generation output of the energy system to the maximum output the system is rated to generate over any given timeframe.

Nitrate Feedstock

For our modelling purposes, we consider that the NO_x emissions from coal-based power plants will provide the required nitrate ions for electrolysis. Jiang et al. carried out an analysis of a solvent based system to capture emissions from the flue gas mixture (containing 250 ppm NOx).[13] The system was designed to capture 99% of NO_x present in 560 ton h^{-1} flue gas by dissolving the NO_x in $NaClO_2$ solvent to produce nitric acid (NO_3^- ions), which can then be recovered with high purity and concentration via heating at 55°C at atmospheric pressure. To simplify, we assume NO_3^- concentration recovered from the capture unit matches the requirement for the electrolyser. Jiang et al. estimated the capture cost to be \$46.2 per tonne of CO_2 captured (inclusive of pressure, temperature and compression requirements), hence we used this basis to determine the NO_x capture cost using the molar balance of the flue gas, calculated as \$315 per ton.

Flue Gas System Capture Cost:
Reference Capture Cost *= \$46.2 ton_{CO2}^{-1}*
Molar Balance of Captured Flue Gas:
Total Flue Gas Flowrate *= 560 $ton_{CO2}\ hr^{-1}$*
Note: For Simplification we assume that the CO_2 flowrate is the flowrate of total flue gas.
Molar Flow Rate of Flue Gas *= 12,727,272.73 mol hr^{-1} (@44.01 g mol^{-1} of CO_2)*
Molar Flowrate of NO_x in Captured Flue Gas:
Molar Flowrate of NO_x = *3,181.82 mol hr^{-1} (@250 ppm of NO_x = 0.025% by vol.)*

Molar Flowrate of NO_x = *0.15 ton hr^{-1} ((@46.01 g mol^{-1} of NO_2)*

Capture Cost of NO_x:

NO_x Capture Cost *= \$46.2/0.15 = 315 \$ per ton NO_x.*

Water Feedstock

A water cost of \$0.02 L^{-1} is considered for our study.[8]

Electrolyser Maintenance

We assume that the electrolyser operation and maintenance cost (O&M) is 3.2% of the electrolyser capital cost per year. We also consider that the PEM electrolyser stacks have a limited life of 60,000 hours after which it must be replaced, at a cost of 15% of the electrolyser system cost.[10] Depending on the capacity factor the electrolyser is operated, these 60,000 hours were distributed over the operational years (e.g. for grid system at a capacity factor of 97%, the stack replacement will be due after every 7 years of operation).

C. Economic Opportunity with NO_xRR

The scalability of NO_xRR depends on the availability of NO_x feedstock. Recent reports by the environmental agencies of United States and Australia reveal NO_x emissions of ~3,000 kton yr^{-1} (for US in 2019)[14] and 521 kton yr^{-1} (for Australia in 2020),[15] from power plants and industry. In fact, even under the most optimistic energy infrastructure transition to a clean energy scenario, IEA projects that 10% of global energy supply in 2040 will be from coal power plants, which is a major NO_x emitter.[16] Apart from power sector, industry such as steelmaking and cement kilns are point sources of NO_x.[17–19] IEA has projected that ~21.7 Mt of NO_x emissions were generated by industry sources in 2015.[20] Non-conventional sources such as wastewater and agricultural waste are also NO_x sources due to biological activity and fertilizer decomposition in soil, respectively.[21] Further, the emerging hydrogen economy is seeing increased deployment of renewable ammonia as fuel for combustion (co-fired with coal), which can generate NO_x as byproduct from partial oxidation.[22,23] These statistics and market direction clearly outline significant opportunity in implementing NO_xRR for environmental mitigation, generate fuels and enable a circular economy.

Another aspect to improving the economics of this P2X pathway would be the NO_x feedstock costs and this this has been overlooked by other recent studies.[24,25] Though a robust model for NO_x capture system costs was not included in the scope of our work, we provide an analysis on LC_{NH4^+} at different possible NO_x costs (**Figure S10a**). This reduction in NO_x feedstock cost can be attained through improvement in capture technologies such as gas scrubbing and pressure swing adsorption.[26] In addition, the eventual cost of NO_x capture will also depend on the NO_x levels in the flue gas. Whilst we do not analyse this effect of NO_x concentration on capture cost, similar analysis with carbon capture technologies shows that CO_2 concentration in flue gas greatly dictates eventual capture costs for gas scrubbing and adsorption.[27,28] Thus, future work should focus on identifying key high concentration NO_x sources and how that may influence NO_xRR. Nevertheless, the cost of systems for NO_x abatement similar to other carbon capture technology are projected to experience rapid cost reductions with learning rates of 10 – 12% expected.[29]

3. Supporting Figures

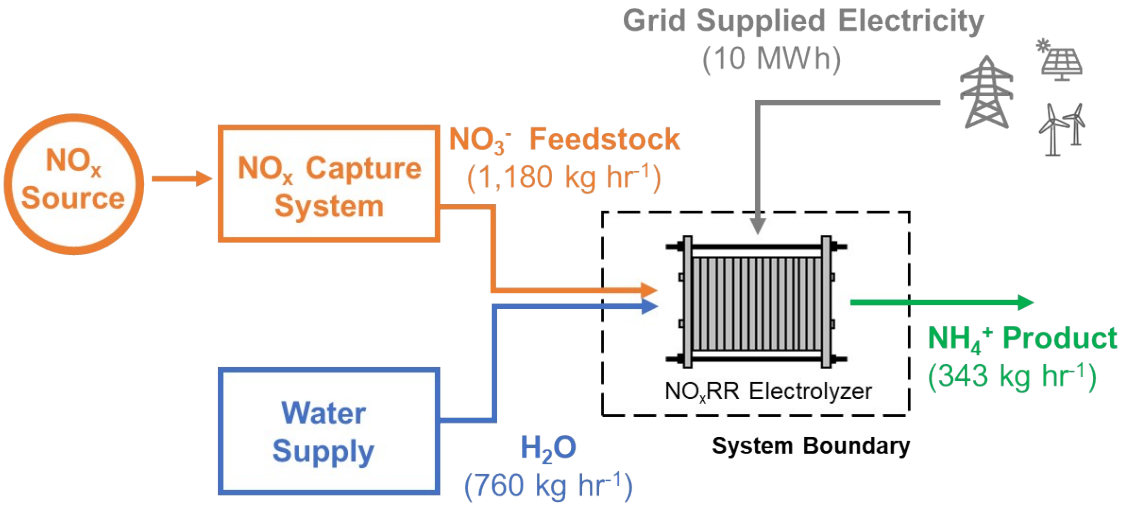

Figure S1. Process flowsheet considered for economic modelling. Note that the key focus of this work is in evaluating the improvement in NO_xRR feasibility as a Renewable Power-to-X pathway to generate green NH_3 from improvement in catalysis performance through oxygen vacancy engineering. NO_x, water and electricity are considered as feedstock inputs and the values will change for different cell voltage and current density.

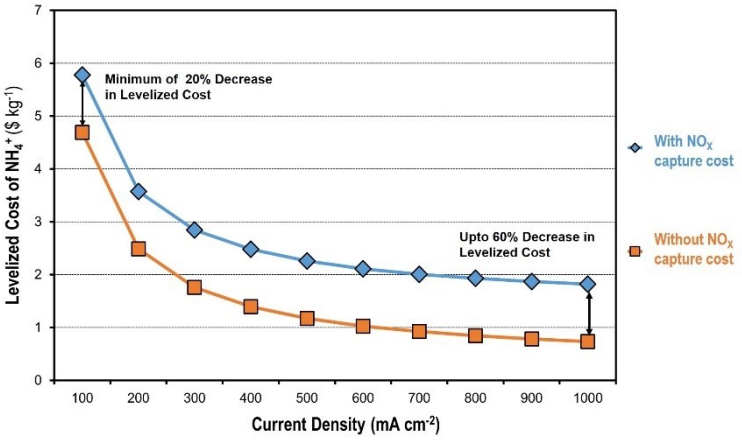

Figure S2. Impact of levelized cost of NH_4^+ as a function of NO_x capture cost and current density at an electricity cost of \$97 MWh^{-1} and electrolyser capacity factor of 97% operating at a cell voltage of 2.2 V. From these results, it is clear that LC_{NH4}^+ can be reduced if NO_x capture costs can be improved through R&D or by combining CO_2 and NO_x capture in a single hub to take advantage of economics of scale. Note that this analysis was carried out with the assumption of NH_4^+ production rate of 600 g m^{-2} h^{-1} (DOE target).

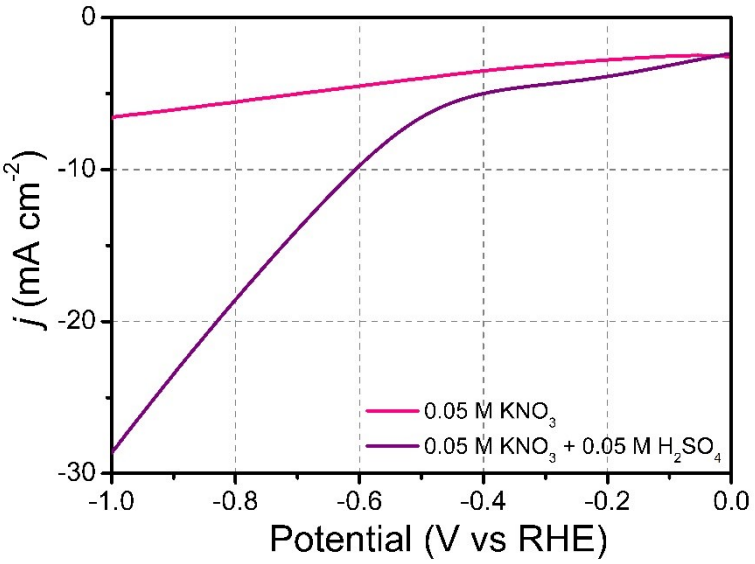

Figure S3. Optimization of electrolyte for NO_xRR with background Cu Foam electrode. The polarization curves indicate an improvement in *j* with a slight addition of H_2SO_4. This addition of acid improves the ionic conductivity of the electrolyte as well as providing H^+ ions that are necessary for the NO_3^- to NH_4^+ reaction mechanism:

$$NO_3^- + 10H^+ + 8e^- \rightarrow NH_4^+ + 3H_20 \qquad E^0 = 0.93\ V\ vs\ RHE \qquad (8)$$

$$NO_3^- + 2H^+ + 2e^- \rightarrow NO_2^- + H_2O \qquad E^0 = 1.02\ V\ vs\ RHE \qquad (9)$$

$$NO_2^- + 8H^+ + 6e^- \rightarrow NH_4^+ + 2H_2O \qquad E^0 = 0.86\ V\ vs\ RHE \qquad (10)$$

$$2H^+ + 2e^- \rightarrow H_2 \qquad E^0 = 0\ V\ vs\ RHE \qquad (11)$$

A suitable amount of H^+ can facilitate the hydrogenation of *NO to *NOH and subsequent hydrogenation of *NOH to $*NH_2OH$ that is then converted to $*NH_4^+$. Our control experiments with Cu foam reveal that in absence of acid, the NH_4^+ yield decreases significantly from 35 $\mu molcm^{-2}h^{-1}$ (in presence of acid) to 7 $\mu molcm^{-2}h^{-1}$ (no acid) during electrolysis at -0.8 V, confirming that the acid provides both protons and chemical bias for the NO_xRR reaction. Note that a higher concentration of acid leads to decreased NH_4^+ selectivity owing to competing hydrogen evolution reaction (HER).[30]

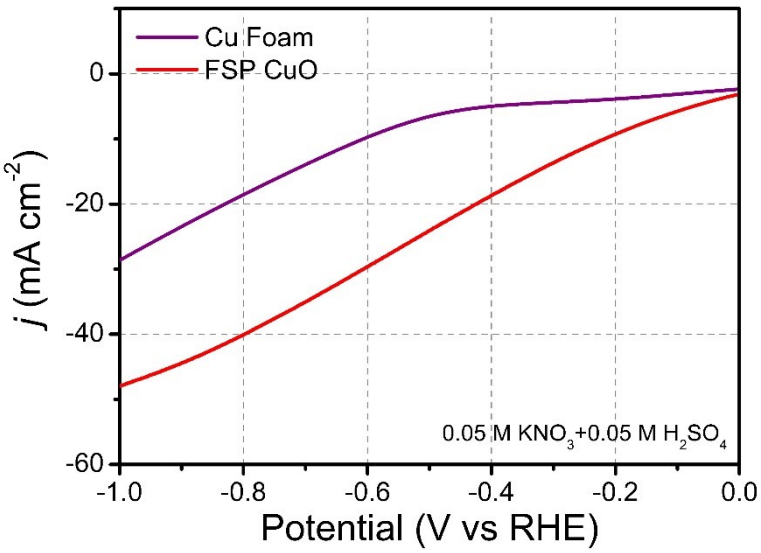

190

Figure S4. NO_xRR polarization curves for FSP CuO and Cu Foam in 0.05M KNO_3+0.05 M H_2SO_4. The curves reveal a higher *j* with FSP CuO when compared to background Cu Foam.

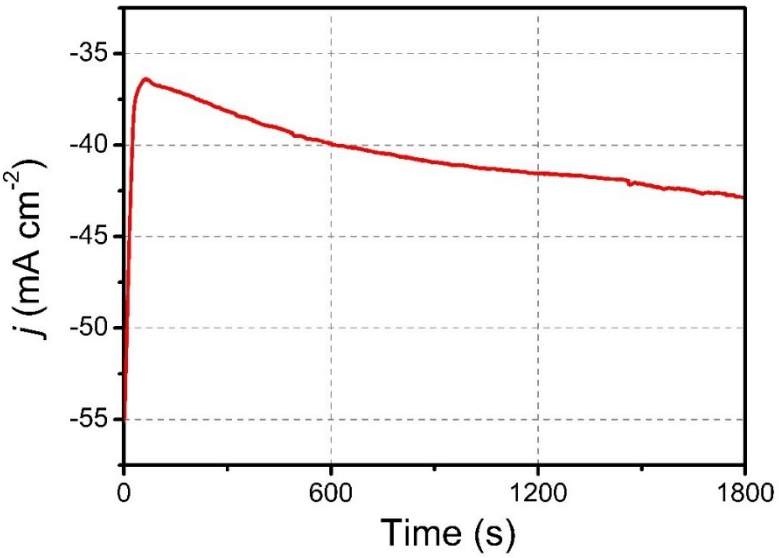

195 **Figure S5.** Representative chronoamperometric *i*-t curve for FSP CuO at -0.8 V for 30 minutes electrolysis duration in 0.05M KNO_3+0.05 M H_2SO_4. Note that there is a slight change in *j* arising from consumption of NO_3^- and H^+ and formation of NH_4^+, thereby changing electrolyte conditions.

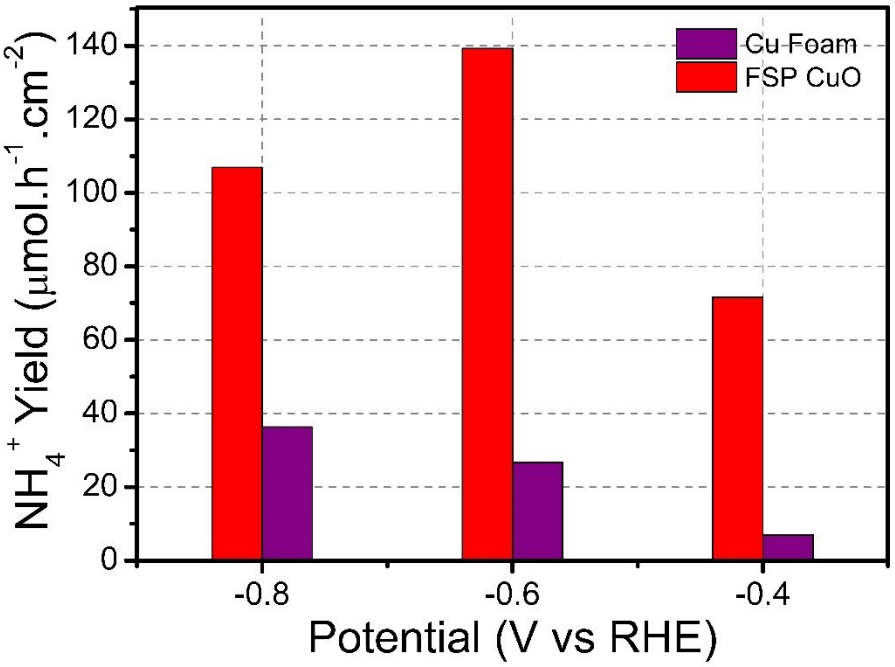

200

Figure S6. Dependence of NH_4^+ yield on applied potential for FSP CuO and Cu Foam in 0.05M KNO_3+0.05 M H_2SO_4. The results reveal a much higher NH_4^+ yield with FSP CuO when compared to Cu Foam.

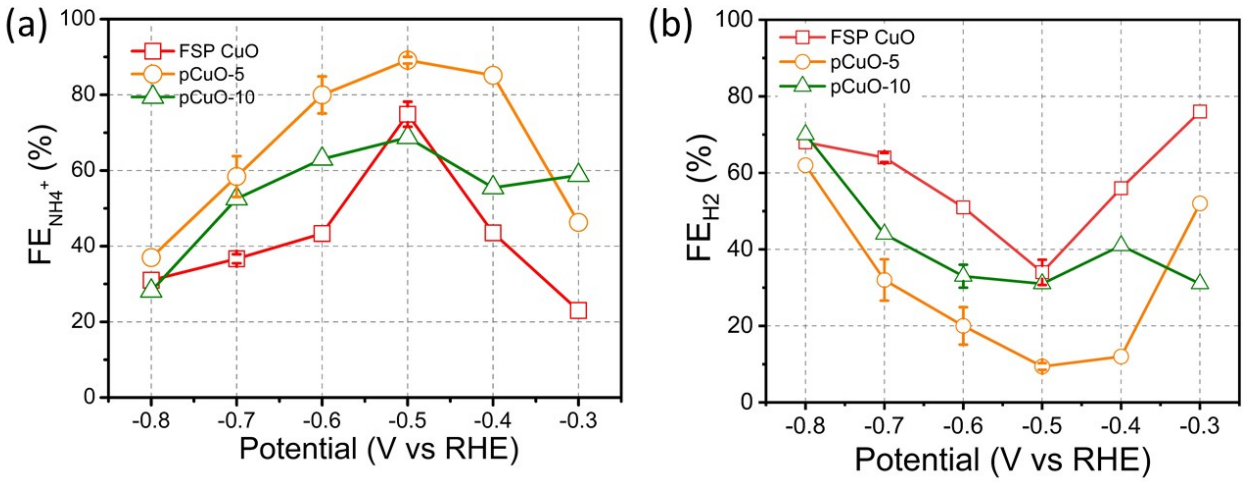

Figure S7. Dependence of **(a)** FE_{NH4^+} and **(b)** FE_{H2} on applied potentials for FSP CuO, pCuO-5 and pCuO-10 in 0.05M KNO_3+0.05 M H_2SO_4. The trends reveal that suitable plasma treatment of 5 minutes with FSP CuO is leading to an improvement in FE_{NH4^+} and a decline in FE_{H2}. Further increase in plasma duration to 10 minutes leads to a decrease in FE_{NH4^+}. The maximum FE_{NH4^+} of FSP CuO, pCuO-5 and pCuO-10 are 72%, 89% and 69% at an applied potential of -0.5 V vs RHE, respectively. Note that apart from H_2, we do not observe any other byproduct.

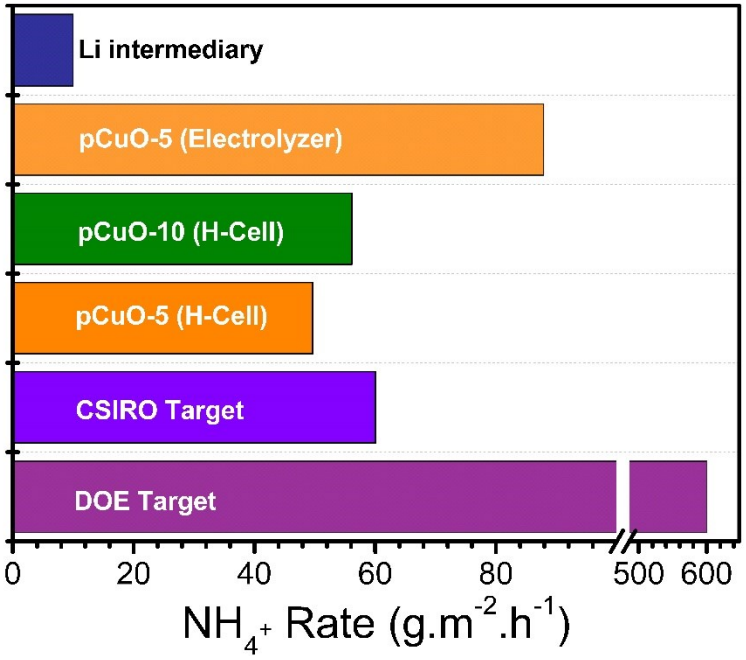

Figure S8. Benchmarking of NH_4^+ yield activity with DOE and CSIRO target (for eNRR) and literature for intermediary NH_3 pathways. It is clear that NH_4^+ yield with pCuO-5 is higher than best-reported Li intermediary performance and the CSIRO target. Note that the performance is lower than the DOE target, highlighting further opportunity with catalyst design.[31–33] Note: that there are no current benchmarks set for direct nitrate reduction to ammonia pathway.

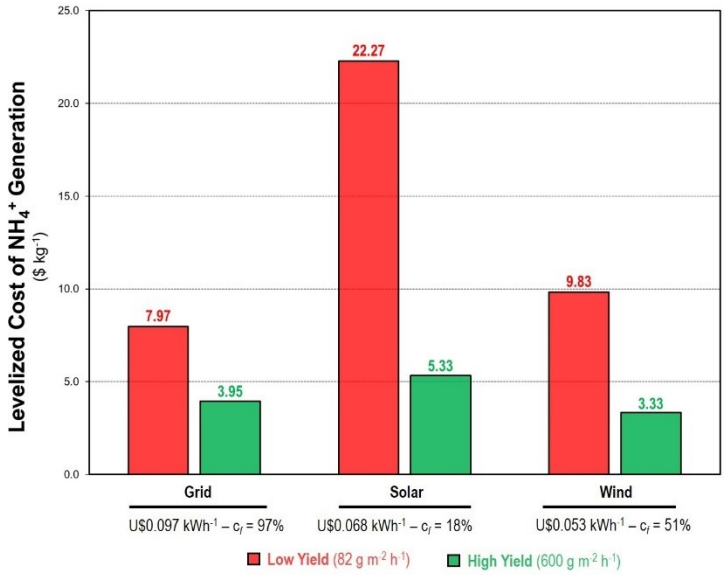

Figure S9. Levelized cost of NH_4^+ under different global electricity supply configurations. At low yield (pCuO-5 results), the grid PPA configuration is the most economical scenario for operating NO_xRR system whereas for the high yield scenario, wind driven electrolyser configuration presents the lowest LC_{NH4}^+.

Note: the variation in levelized costs among the different configuration results from changing electricity pricing and capacity factor, which affect the amount of NH_4^+ being generated. For pCuO-5, the levelized cost for NH_4^+ generation can be reduced by increasing the absolute amount of NH_4^+ being generated by operating the electrolyser at a higher capacity factor, even at a higher electricity price. For this reason, the LC_{NH4}^+ for pCuO-5 attained with grid configuration presents the lowest cost. In comparison, for target yield catalyst (production rate of 600 g $m^{-2}h^{-1}$), the LC_{NH4}^+ is more influenced by electricity pricing and therefore operating the electrolyser with wind PPA, which presents the lowest electricity pricing and moderate capacity factors (~51%) presents a lower LC_{NH4}^+ than compared to grid (with high price but high capacity factor).

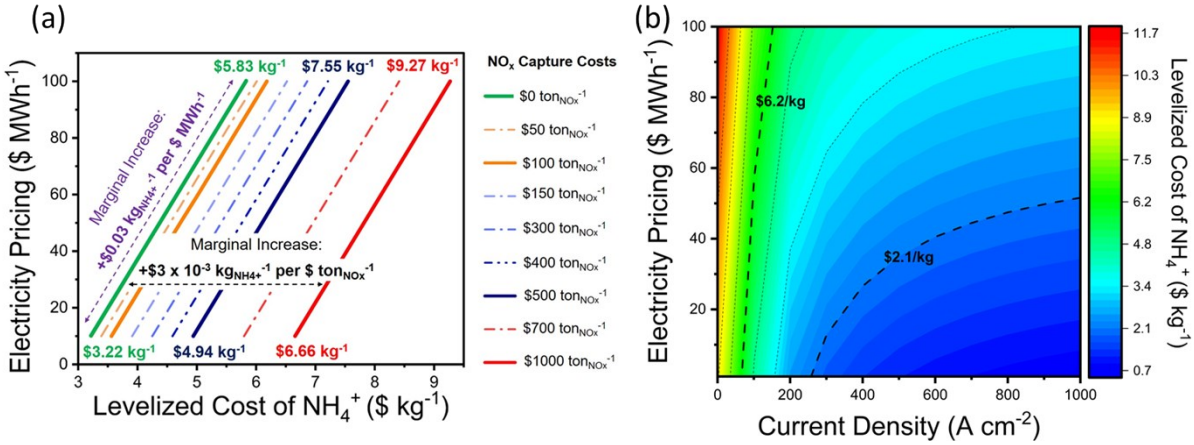

Figure S10. (a) The influence of NO_x capture costs on LC_{NH4}^+. The analysis was conducted for a fixed cell voltage of 2.2 V and current density of 150 mA cm^{-2} at under the technoeconomic assumptions. The shown marginal increase represents the change in LC_{NH4}^+ ($ kg_{NH4}^+) per unit increase in electricity price (Purple dotted line) and NO_x feedstock costs (Black dotted line). As observed the cost of electricity plays a more dominating role on the LC_{NH4}^+ when compared to the NO_x feedstock costs. **(b)** Economic modelling of NO_x conversion to NH_4^+ using pCuO-5 in a 10 MW electrolyser system (without NO_x capture costs).

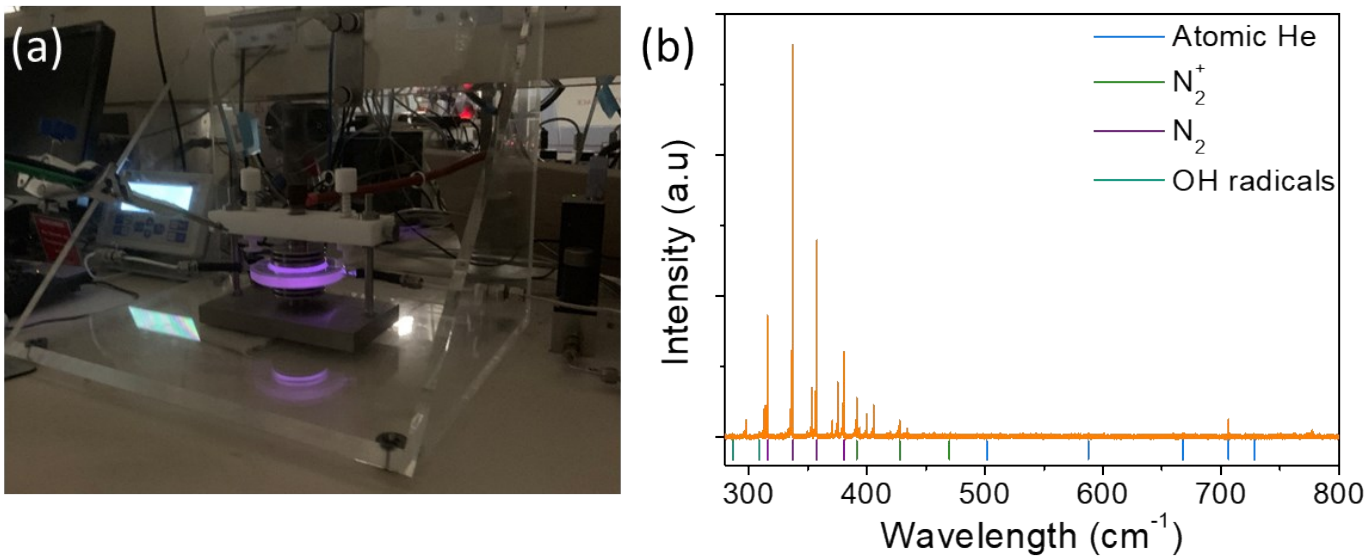

Figure S11. (a) Digital image of *in-situ* OES measurements. **(b)** *In-situ* OES spectra during plasma-treatment of FSP CuO for 10 minutes.

245

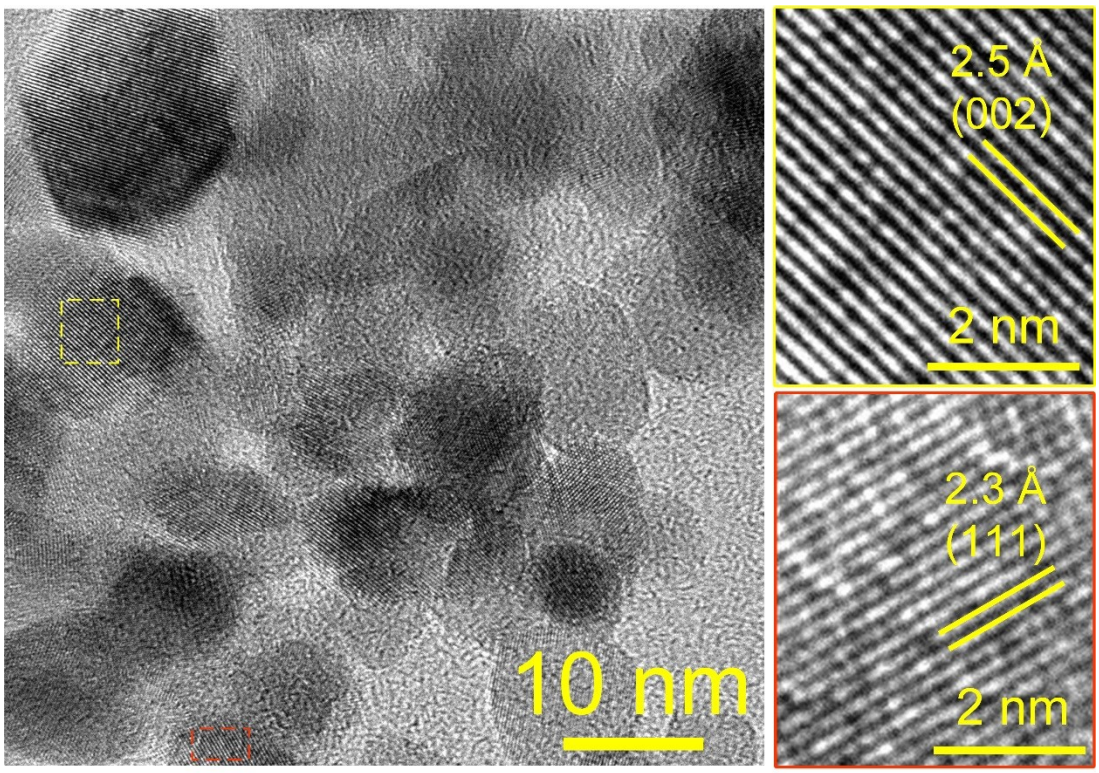

Figure S12. TEM and HRTEM images of FSP CuO. The TEM image reveals formation of anisotropic particles with a particle size of ~10 nm. The corresponding HR-TEM images reveal lattice fringes indicating the formation of CuO {111} and {002} facets.

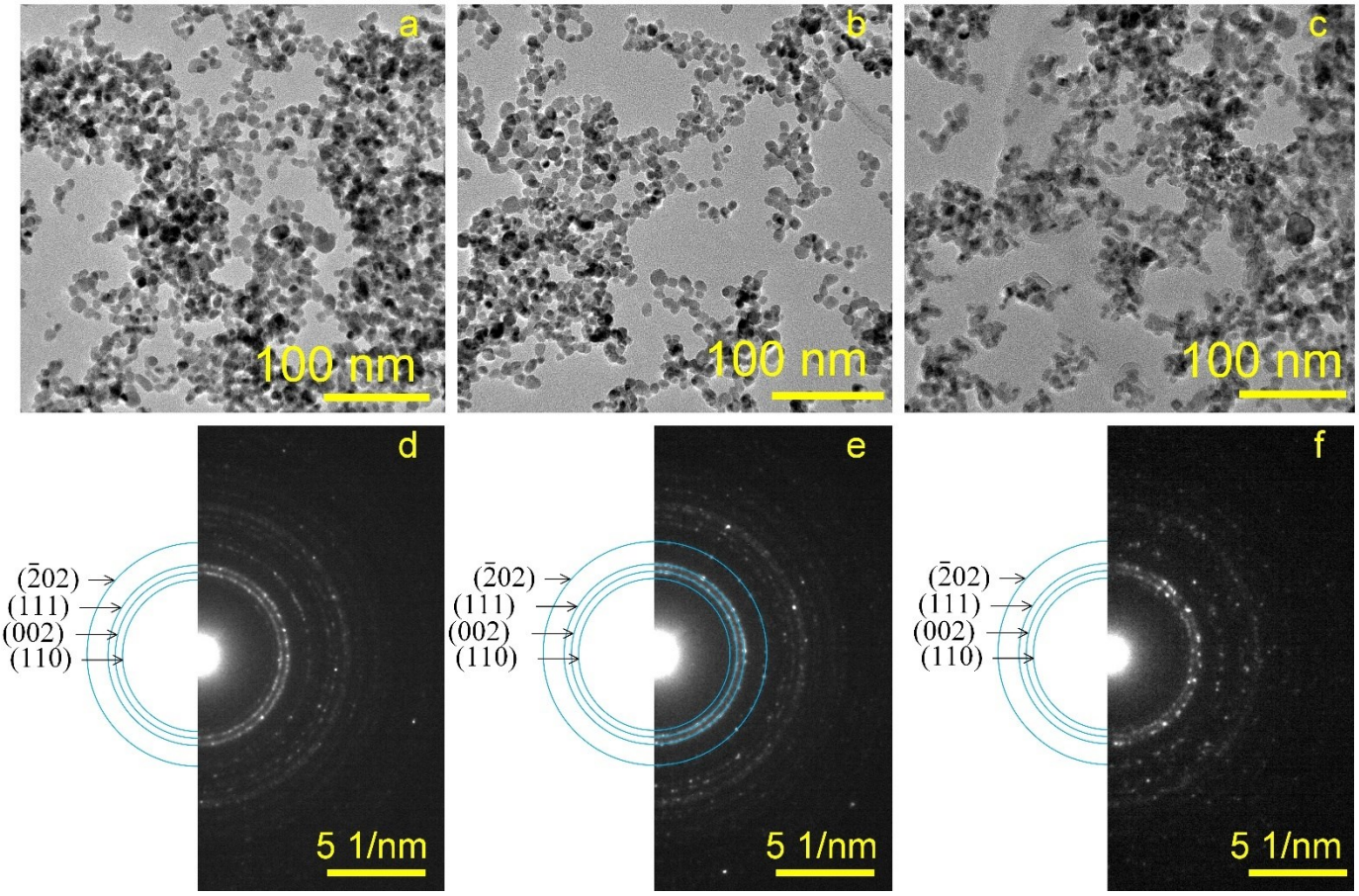

Figure S13. TEM images and corresponding selected electron area diffraction pattern for **(a,d)** FSP CuO, **(b,e)** pCuO-5 and **(c,f)** pCuO-10. The intensity of electron diffraction patterns for pCuO-10 is lower than that attained with pCuO-5.

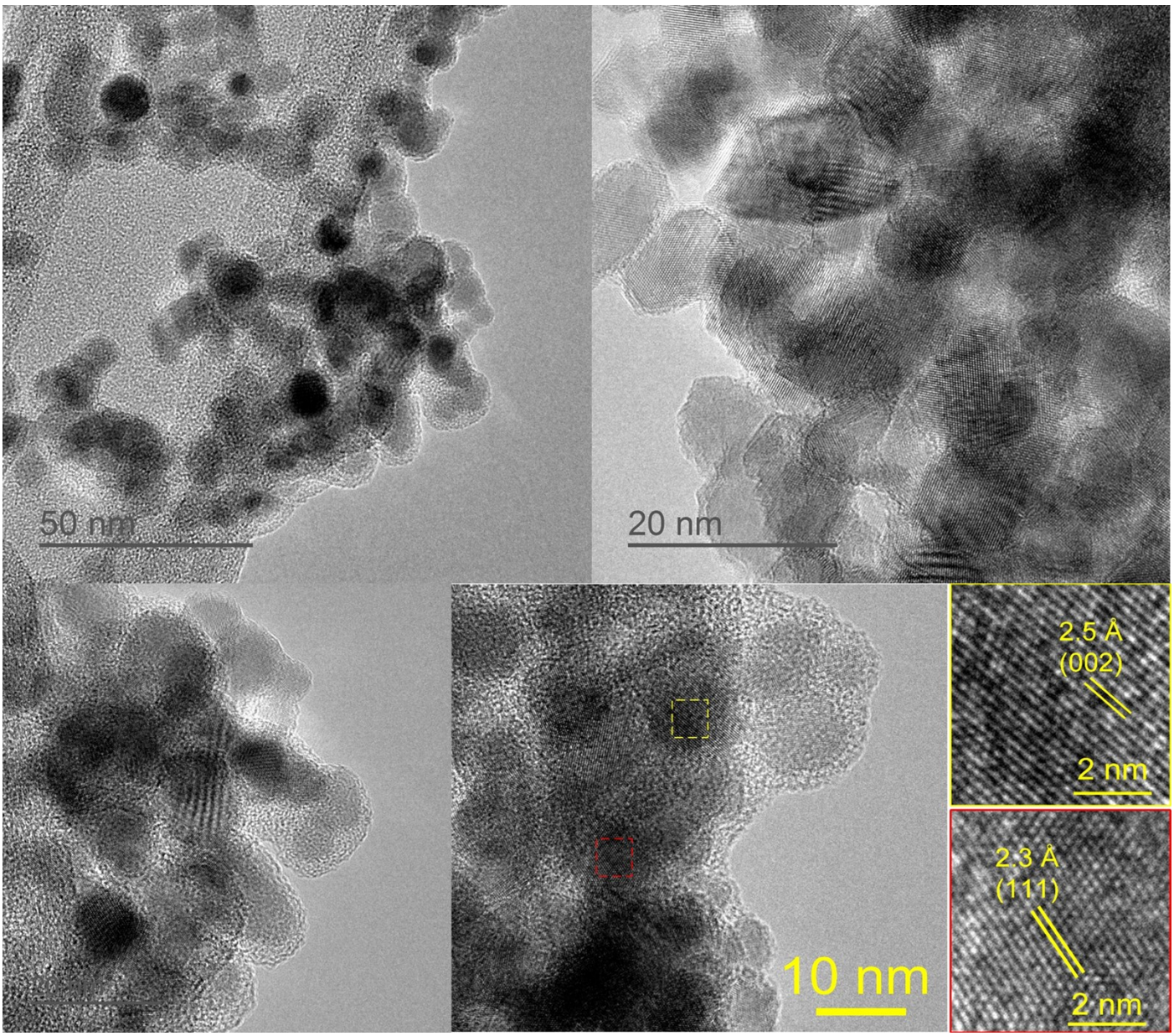

Figure S14. TEM and HR-TEM image of pCuO-10. The surface of the catalyst is less crystalline (compared to FSP CuO and pCuO-5).

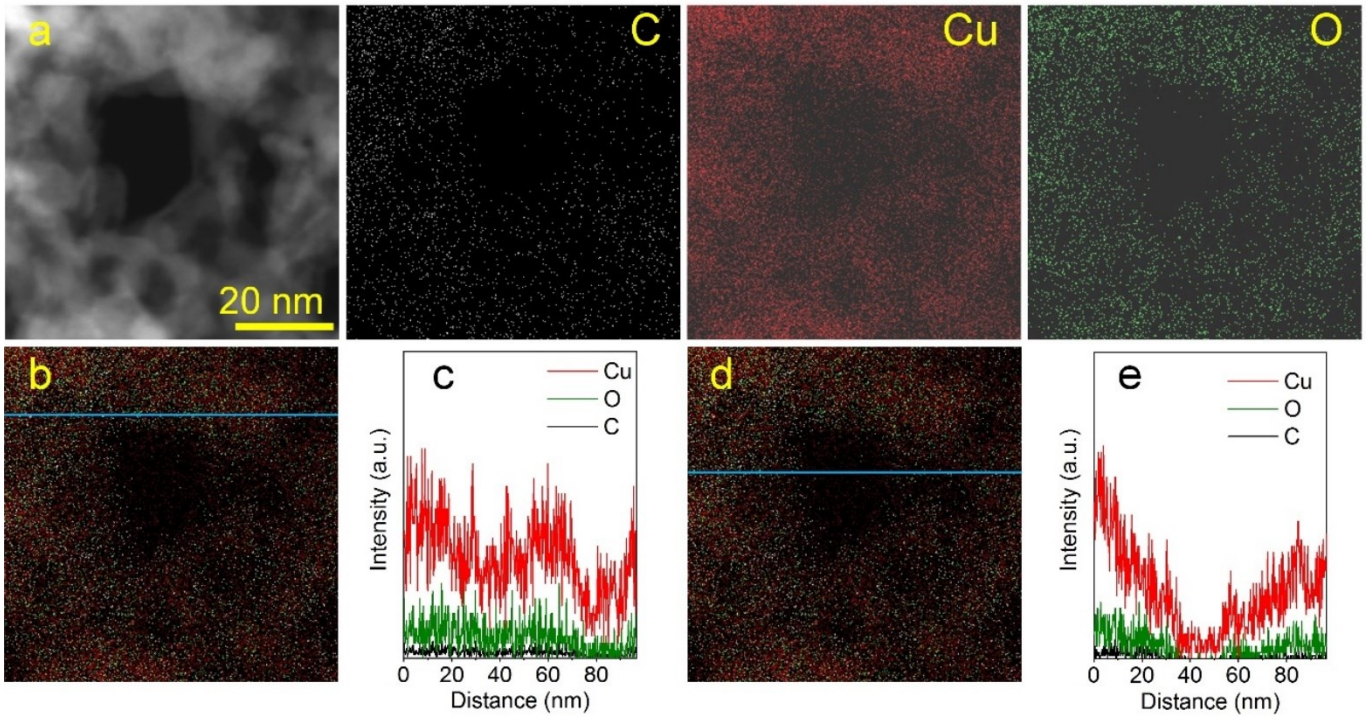

Figure S15. EDX mapping of pCuO-10. **(a)** TEM imaging and corresponding EDX mapping showing the presence of Cu, O and C. **(b,d)** Line scan direction from left to right and the **(c,e**) corresponding spectra. Note that the presence of C can be from the background as well as residual C moieties generated during FSP synthesis.

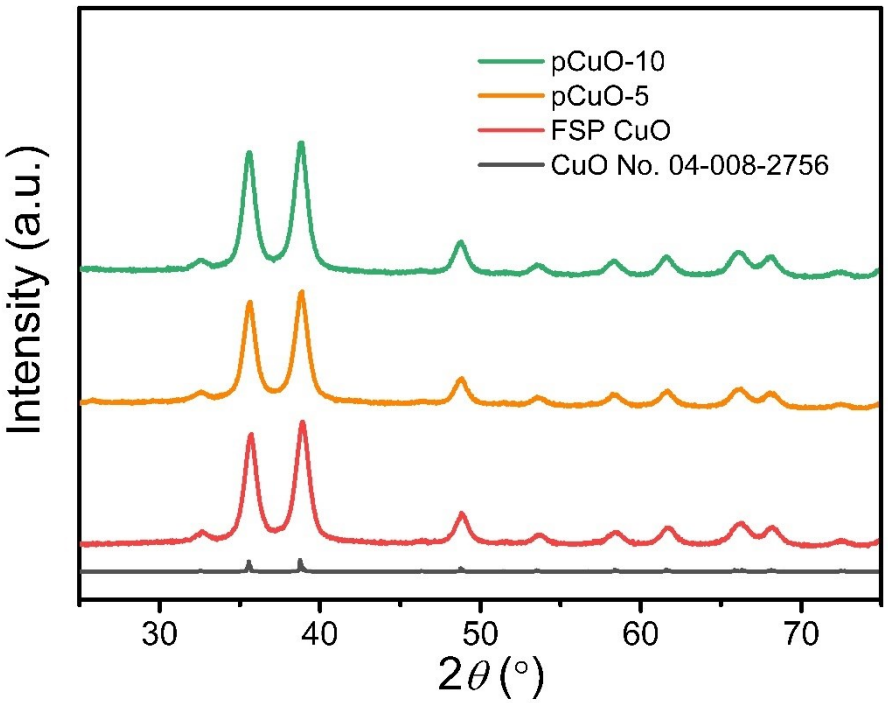

Figure S16. XRD patterns for FSP CuO, pCuO-5 and pCuO-10. The XRD patterns with FSP CuO, pCuO-5 and pCuO-10 revealed major peaks at 32°, 35°, 38.8°, 48.7°, 66° and 68°, which correspond to the {110}, {002}, {111}, $\{\bar{2}02\}$, $\{\bar{3}11\}$ and {220} reflections of CuO (JCPDS 04-008-2756). The XRD patterns reveal a similar bulk crystallinity for all the catalysts.

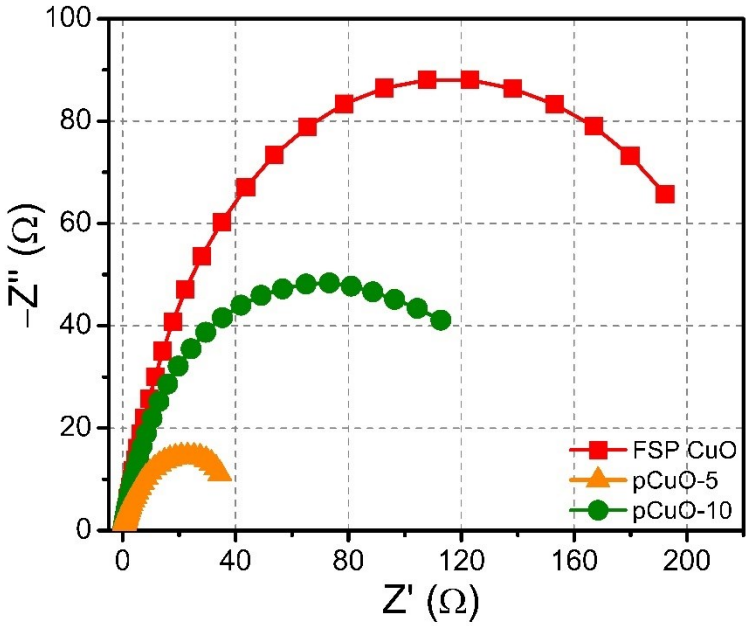

Figure S17. EIS measurements of FSP CuO, pCuO-5 and pCuO-10 at 0.4 V vs RHE in 0.5 M Na_2SO_4. The Nyquist plots indicate that the radius of the semicircle decreases with 5 minutes of plasma-treatment, indicating that the system impedance (electrode conductivity and charge transfer resistance) is improved. However, increasing plasma-treatment duration to 10 minute leads to an increase in system impedance compared to pCuO-5.

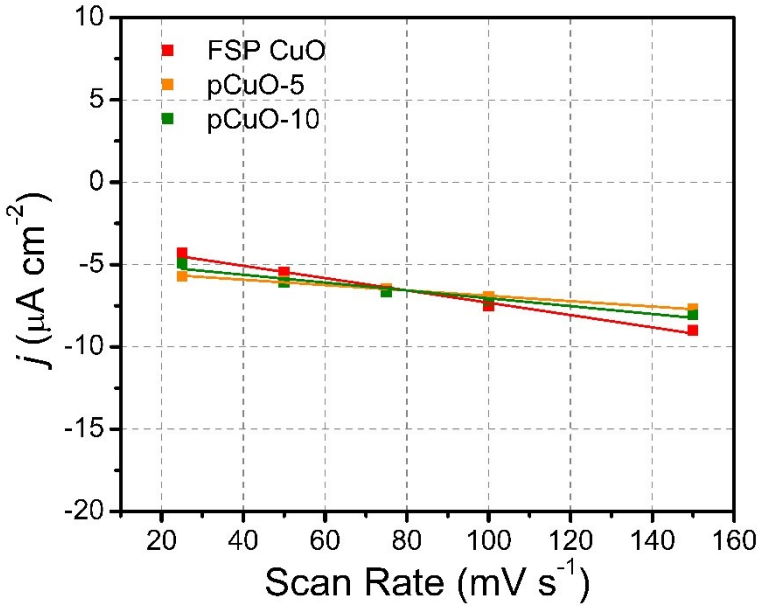

Figure S18. Capacitive current vs scan-rate plots at an applied potential of 0.375 V vs RHE in 0.5 M Na_2SO_4 for FSP CuO, pCuO-5 and pCuO-10. The results reveal a similar electrochemical surface area (ECSA) for all the catalysts.

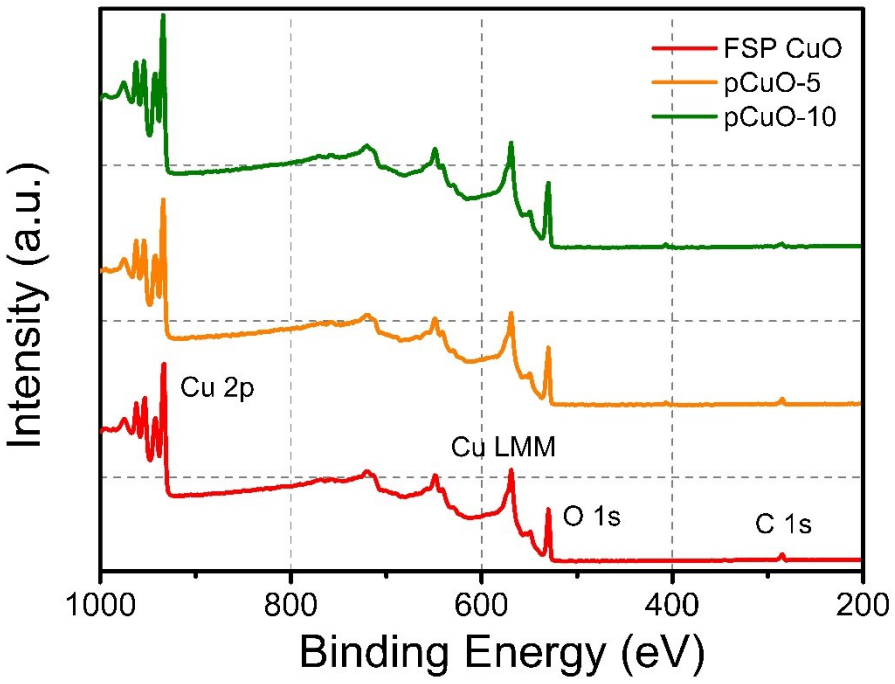

Figure S19. XPS line survey for FSP CuO, pCuO-5 and pCuO-10. It is clear from these results that the samples comprise of Cu and O as well as background C species.

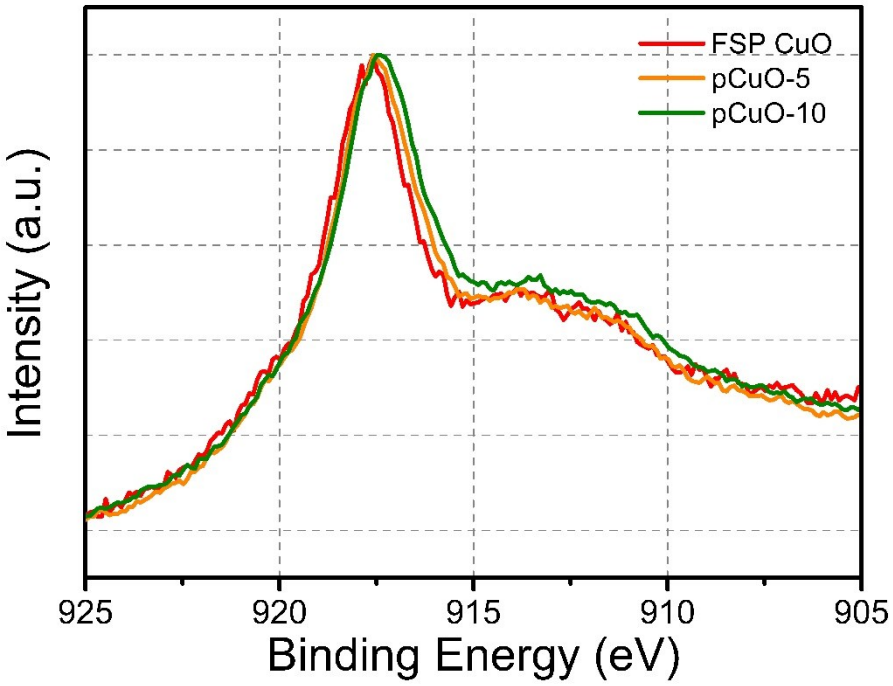

Figure S20. AES profile for FSP CuO, pCuO-5 and pCuO-10. The summation of kinetic energy from AES and summation of binding energy for peaks from high-resolution Cu 2p spectra indicate that the predominant oxidation state on the surface of all the catalyst is Cu^{2+}.[34]

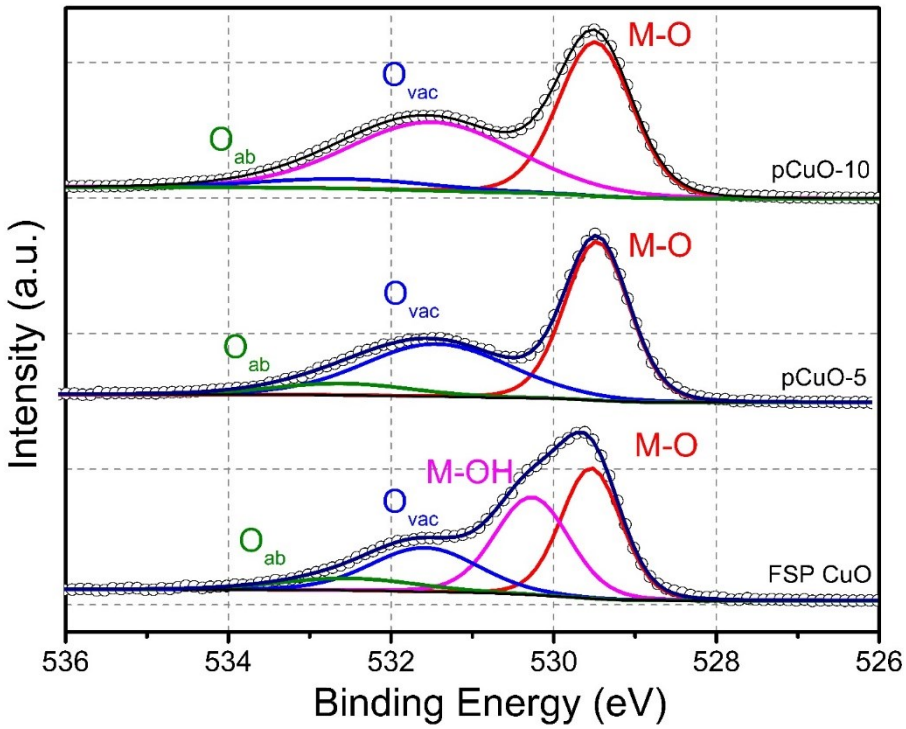

Figure S21. High-resolution O1s spectra for FSP CuO, pCuO-5 and pCuO-10. M-O, M-OH, O_{vac} and O_{abs} refer to metal-oxygen, metal-hydroxide, signals arising from oxygen vacancy and absorbed oxygen, respectively. We note that all catalysts display prominent peak at binding energy 529.5 eV that corresponds to formation of Cu^{2+} within the catalysts. FSP CuO displays a peak at binding energy 530.7 eV that correspond to presence of $Cu(OH)_2$, which transforms to oxide moieties during plasma treatment. Given that XRD patterns do not indicate any peaks corresponding to $Cu(OH)_2$, we believe this hydroxide species formed during FSP to be of thin layer/amorphous nature and it transforms to oxide moieties during plasma-treatment.[35]

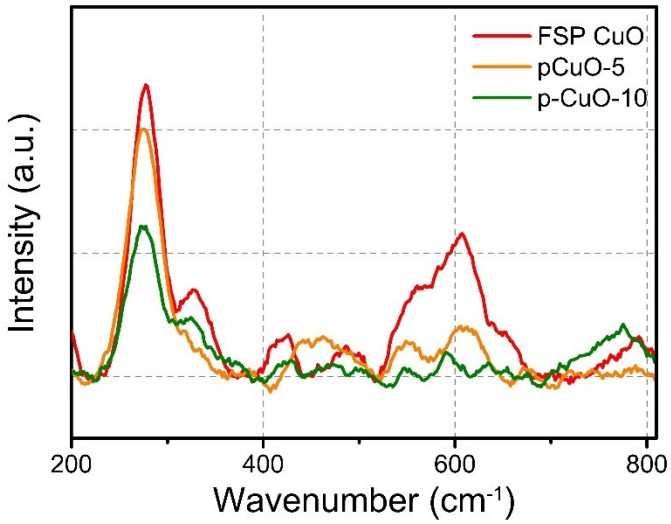

Figure S22. Raman spectra for FSP CuP, pCuO-5 and pCuO-10. The Raman spectra reveals a sharp peak at wavenumber 290 cm^{-1} which corresponds to A_g vibration modes of CuO as well as peaks at 328 cm^{-1} and 608 cm^{-1} that correspond to B_g vibration modes of CuO.

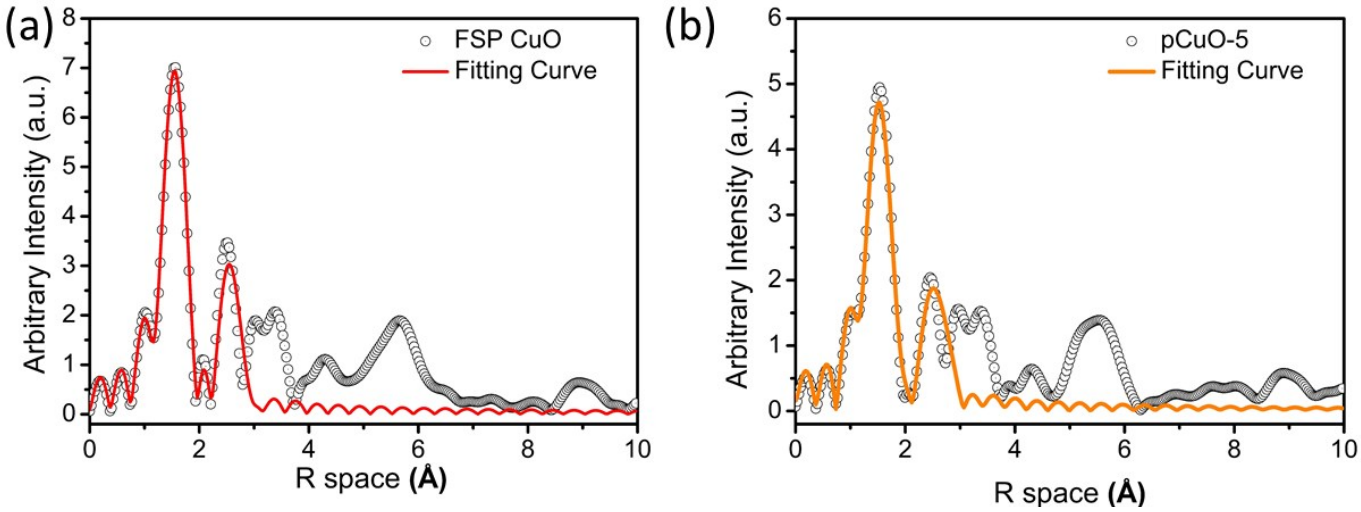

Figure S23. Fitting results for **(a)** FSP CuO and **(b)** pCuO-5.

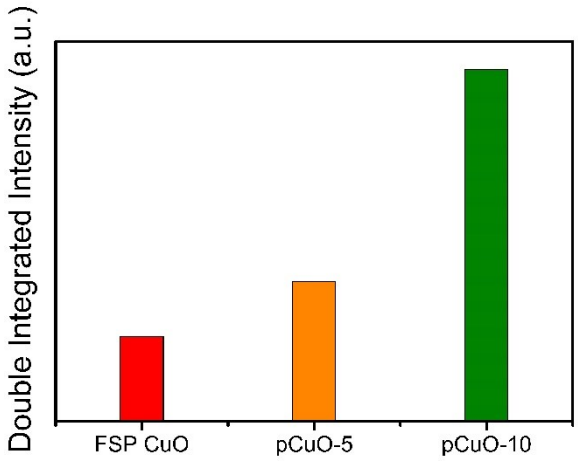

Figure S24. Double integrated intensity of EPR spectra for FSP CuO, pCuO-5 and pCuO-10 at g value of 2.002. Note that the experimental EPR spectrum is the first derivative of absorption with respect to the applied magnetic field. We carry out double integration to estimate the area under the EPR signal and this is proportional to the number of spins and amount of defects.[36]

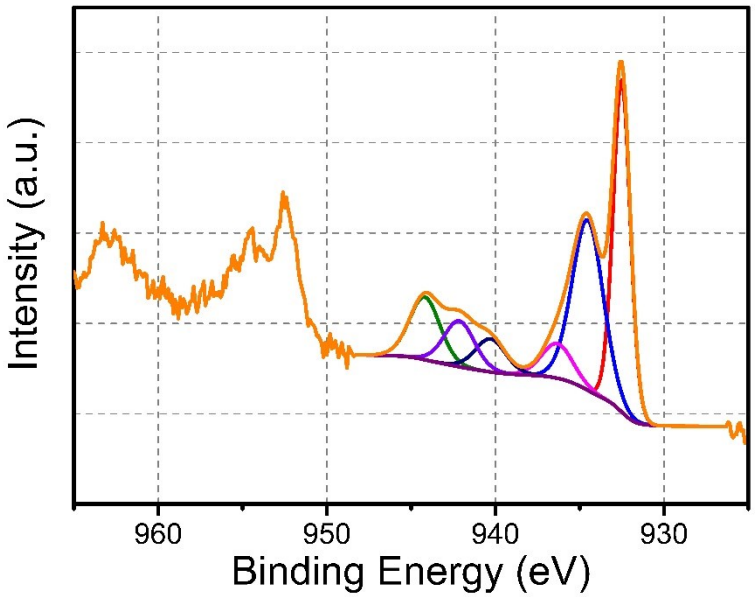

Figure S25. High-resolution Cu 2p XPS spectra for post-reaction pCuO-5 electrode. The spectra reveal the formation of Cu_2O on the surface of the electrode owing to the negative bias applied during NO_xRR and are in agreement with *operando* Raman measurements (**Figure 4b**). Note: the surface of the electrode is prone to oxidation and for testing, the post-reacted electrode was kept in a desiccator prior to XPS measurements.

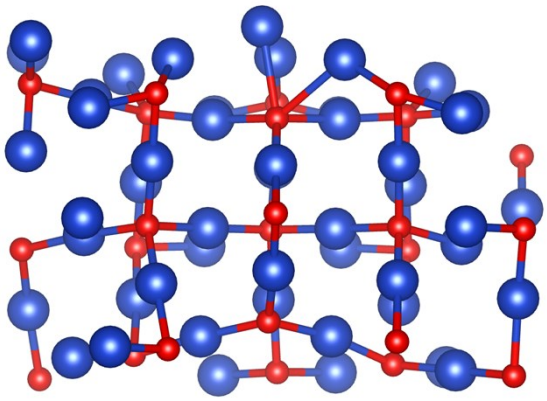

320

Figure S26. Pristine Cu_2O (111) terminated model used for DFT modelling.

4. Supporting Tables

Table S1 summarizes the technoeconomic parameters used in this study which is used to calculate the levelized cost of ammonium generated as our techno-economic metric, as shown in the equation below:

$$Levelized\ Cost\ of\ Ammonium\left(\frac{\$}{kg}\right) = \frac{R_f \times (CAPEX) + OPEX}{Product\ Generated} \quad (12)$$

Here, R_f represents the capital recovery factor, the CAPEX and OPEX represent the capital and operating costs of the electrolyser system.

Table S1. Technoeconomic Parameters

Parameter	Assumption
Economic Parameters	
Currency Basis	USD$ - 2020
Project Life	20 years
Recovery Factor	0.08% (For a nominal weighted average capital cost of 4.5%)
Electrolyser System	
Electrolyser Power	0.1 – 10 MW
Current Density	0 – 1000 mA cm^{-2}
Voltage	1.7 – 2.3 V
Lifetime	20 Years
Capacity Factor (c_f)	Depending on the electricity source
Electrolyser Capital Cost	
Reference costs	DoE: \$342 kW^{-1}
Electrolyser Operating Cost	
Electricity Consumption cost	\$97 MWh^{-1} - (Grid – c_f:97%)
	\$53MWh^{-1} - (Grid – c_f:51%)
	\$68 MWh^{-1} - (Solar PPA – c_f:18%)
Nitrate Consumption Cost	\$315 ton^{-1} of NO_X
Water Consumption Cost	\$0.02 L^{-1}
Electrolyser O&M)	3.2% of electrolyser capital cost per year
Stack Replacement	15% of electrolyser capital cost per replacement

Table S2. EXAFS fitting results of FSP CuO.

path	N	σ^2 (Å^2)	R (Å)	R factor
O	1.948	0.00202	1.952	0.0083
Cu	4.000	0.01906	2.906	

335 **Table S3.** EXAFS fitting results for pCuO-5.

path	N	σ^2 (Å^2)	R (Å)	R factor
O	2.136	0.0074	1.960	0.0073
Cu	3.652	0.022	2.881	

5. References

1 G. Kresse and D. Joubert, *Phys. Rev. B*, 1999, **59**, 1758–1775.

2 G. Kresse and J. Hafner, *Phys. Rev. B*, 1994, **49**, 14251–14269.

3 G. Kresse and J. Furthmu, *Phys. Rev. B*, 1996, **54**, 11169–11186.

4 J. P. Perdew, K. Burke and M. Ernzerhof, *Phys. Rev. Lett.*, 1996, **77**, 3865–3868.

5 A. a. Peterson, F. Abild-Pedersen, F. Studt, J. Rossmeisl and J. K. Nørskov, *Energy Environ. Sci.*, 2010, **3**, 1311.

6 Y. Zhou, W. Chen, P. Cui, J. Zeng, Z. Lin, E. Kaxiras and Z. Zhang, *Nano Lett.*, 2016, **16**, 6058–6063.

7 S. Guo, K. Heck, S. Kasiraju, H. Qian, Z. Zhao, L. C. Grabow, J. T. Miller and M. S. Wong, *ACS Catal.*, 2018, **8**, 503–515.

8 M. Jouny, W. Luc and F. Jiao, *Ind. Eng. Chem. Res.*, 2018, **57**, 2165–2177.

9 J. Na, B. Seo, J. Kim, C. W. Lee, H. Lee, Y. J. Hwang, B. K. Min, D. K. Lee, H. S. Oh and U. Lee, *Nat. Commun.*, , DOI:10.1038/s41467-019-12744-y.

10 D. Peterson, J. Vickers and D. DeSantis, *DOE Hydrog. Fuel Cells Progr. Rec.*

11 IEA, *Energy Prices 2020*, IEA, Paris, 2020.

12 */publications/2020/Jun/Renewable-Power-Costs-in-2019*.

13 K. Jiang, H. Yu, L. Chen, M. Fang, M. Azzi, A. Cottrell and K. Li, *Appl. Energy*, 2020, **260**, 114316.

14 United States Environmental Protection Agency, in *Draft U.S. Greenhouse Gas Emissions and Sinks (1990 - 2019)*, EPA, Washington, DC, EPA 430-R-., 2021.

15 W. and the E. Australian Government Department of Agriculture, National Pollutant Inventory.

16 IEA, *World Energy Outlook 2019*, IEA, Paris, 2019.

17 X.-Z. Feng, O. Lugovoy and H. Qin, *Adv. Clim. Chang. Res.*, 2018, **9**, 34–42.

18 S. Zhang, H. Ren, W. Zhou, Y. Yu and C. Chen, *J. Clean. Prod.*, 2018, **185**, 761–771.

19 P. Cavaliere and A. Silvello, *Ironmaking and Steelmaking Processes*, Springer, 2016, vol. 173.

20 IEA, Emissions of Nitrogen oxyde (NOx) by sector and scenario, 2015 and 2040.

21 G. F. Chen, Y. Yuan, H. Jiang, S. Y. Ren, L. X. Ding, L. Ma, T. Wu, J. Lu and H. Wang, *Nat. Energy*, 2020, **5**, 605–613.

22 T. Komagai, Japan to introduce ammonia for thermal power, shipping fuels in late 2020s.

23 H. Kobayashi, A. Hayakawa, K. D. K. A. Somarathne and E. C. Okafor, *Proc. Combust. Inst.*, 2019, **37**, 109–133.

24 D. Kim, D. Shin, J. Heo, H. Lim, J.-A. Lim, H. M. Jeong, B.-S. Kim, I. Heo, I. Oh, B. Lee, M. Sharma, H. Lim, H. Kim and Y. Kwon, *ACS Energy Lett.*, 2020, 3647–3656.

25 J. M. McEnaney, S. J. Blair, A. C. Nielander, J. A. Schwalbe, D. M. Koshy, M. Cargnello and T. F. Jaramillo, *ACS Sustain. Chem. Eng.*, 2020, **8**, 2672–2681.

26 Y. Sun, E. Zwolińska and A. G. Chmielewski, *Crit. Rev. Environ. Sci. Technol.*, 2016, **46**, 119–142.

27 J. Husebye, A. L. Brunsvold, S. Roussanaly and X. Zhang, *Energy Procedia*, 2012, **23**, 381–390.

28 S. Roussanaly and R. Anantharaman, *Chem. Eng. J.*, 2017, **327**, 618–628.

29 W. Kuckshinrichs and S. Vögele, eds. W. Kuckshinrichs and J.-F. Hake, Springer International Publishing, Cham, 2015, pp. 147–171.

30 J. Sun, D. Alam, R. Daiyan, H. Masood, T. Zhangb, R. Zhoub, P. J., Cullen, Emma C. Lovell, A. (Rouhollah) Jalili and R. Amal, *Energy Environ. Sci.*, , DOI:10.4135/9781446247501.n1321.

31 S. Giddey, S. P. S. Badwal and A. Kulkarni, *Int. J. Hydrogen Energy*, 2013, **38**, 14576–14594.

32 ARPA A-E, *Renewable Energy to Fuels Through Utilization of EnergyDense Liquids (REFUEL)*, 2016.

33 N. Lazouski, M. Chung, K. Williams, M. L. Gala and K. Manthiram, *Nat. Catal.*, 2020, **3**, 463–469.

34 M. Jung, J. N. Hart, J. Scott, Y. H. Ng, Y. Jiang and R. Amal, *Appl. Catal. A Gen.*, 2016, **521**, 190–201.

35 P. Keil, D. Lützenkirchen-Hecht and R. Frahm, *AIP Conf. Proc.*, 2007, **882**, 490–492.

36 C. G. R. Eaton and D. G. Gorenstein, *Bull. Magn. Reson.*, 1988, **10**, 130.